Nano Research

Open Access

Research Article

Ultrathin defect-rich CoFeW-LDH nanosheets with lattice-confined tungsten single atoms for efficient electrocatalytic oxygen evolution reaction

Lingxing Zan[1], Lu Liu[1], Xiaorui Wang[1], Ting Yan[1], Kun Tian[1], Hongling Zhang[1], Xiaohan Cao[1], Delong Wang[1], Yunchuan Tu[2]✉, Jian Li[3], Xin Bo[4], Wenlin Zhang[1]✉, Qingbo Wei[1]✉, and Feng Fu[1]

[1] *Key Laboratory of Chemical Reaction Engineering of Shaanxi Province, College of Chemistry and Chemical Engineering, Yan'an University, Yan'an 716000, China*
[2] *School of Chemistry and Chemical Engineering, Chongqing University, Chongqing 400044, China*
[3] *School of Chemistry and Chemical Engineering, Yulin University, Yulin 718000, China*
[4] *Key Laboratory of Applied Surface and Colloid Chemistry, Ministry of Education, School of Chemistry and Chemical Engineering, Shaanxi Normal University, Xi'an 710119, China*

Cite this article: *Nano Research*, **2026**, *19*, 94908561. https://doi.org/10.26599/NR.2026.94908561

ABSTRACT: High-valence metals play an important role in facilitating the oxidation cycles of 3d metals during the oxygen evolution reaction (OER), while maximizing atomic utilization efficiency is equally vital for further enhancing catalytic activity. Herein, we present a facile strategy to synthesize single-atom W confined within the lattice of CoFe-layered double hydroxide (CoFeW-LDH), which features an ultrathin (~ 5 nm) defect-rich nanosheet-assembled hollow cubic structure that serves as an efficient OER electrocatalyst. The introduction of W, characterized by significant differences in atomic radius and electronic structure, induces numerous lattice defects. This unique geometric structure and the modulated electronic structure endow it with low OER overpotentials of 263 mV at 10 mA·cm^{-2} and remarkable durability exceeding 100 h at a high current density of 1 A·cm^{-2} under alkaline conditions, outperforming most non-precious metal catalysts as well as commercial precious IrO_2 catalyst. Density functional theory calculations reveal that the incorporation of W reconfigures the electronic structure of the adjacent Co sites at defects in a manner conducive to enhancing OER kinetics and charge transfer. This work proposes an effective strategy for synthesizing lattice-confined, high-valence metal single-atom electrocatalysts with enhanced atomic utilization and OER activity.

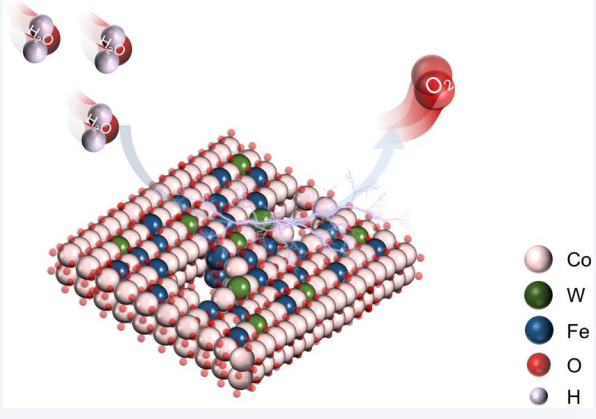

KEYWORDS: CoFeW-layered double hydroxide (CoFeW-LDH), defects, electrocatalysts, high-valence metals, lattice confinement

1 Introduction

Electrocatalytic water splitting has emerged as a highly promising and sustainable strategy for large-scale hydrogen production, offering a clean and renewable energy solution to address global energy issues [1–3]. However, the oxygen evolution reaction (OER), as the anodic half-reaction in electrocatalytic water splitting, involves a sluggish four-electron transfer process, which constitutes the primary bottleneck for efficient hydrogen production via electrolysis [4–6]. Although noble metal-based catalysts, such as ruthenium oxide (RuO_2) and iridium oxide (IrO_2), exhibit high OER activity, their widespread application is limited by the high cost and scarcity of these precious metals [7–9].

In recent years, single-atom catalysts (SACs) have attracted extensive attention in the field of electrocatalysis due to their maximum atomic utilization efficiency, unique electronic structure, and superior catalytic performance [10, 11]. However, the

Received: December 9, 2025; **Revised:** January 26, 2026
Accepted: February 11, 2026

✉Address correspondence to Yunchuan Tu, yctu@cqu.edu.cn; Wenlin Zhang, thuwlzhang@163.com; Qingbo Wei, qbwei@yau.edu.cn

intrinsically high surface free energy of single atoms makes them prone to aggregation during synthesis or catalytic reactions, leading to the formation of nanoparticles or clusters [12, 13]. Once agglomeration occurs, the atomic utilization efficiency decreases significantly, and the distinctive electronic structure of the single-atom active sites becomes distorted, resulting in instability of the catalytic performance [14, 15]. Therefore, it is critical to address the issues of aggregation and leaching of SACs during reactions to ensure their stability [12, 16]. One of the most effective strategies to enhance their stability involves modulating the support structure and the metal–support interaction [17–19]. Layered double hydroxides (LDHs) have been widely used as supports for SACs due to their distinctive advantages, such as well-defined layered two-dimensional structure [20], strong surface anchoring effect [21–23], flexible adjustable composition and electronic structure [24–26]. These characteristics contribute to providing abundant anchoring sites and excellent dispersivity, stabilizing single atoms by preventing their migration and agglomeration, as well as optimizing the electronic structure of active sites, thereby enhancing catalytic performance. In addition, it has been reported that high-valence metal oxides significantly enhance the OER performance, primarily by optimizing the filling of e_g orbitals, promoting efficient charge transfer processes and lattice oxygen migration, inducing valence oscillation of active sites, accelerating surface reconstruction, improving the chemical and structural stability of materials (i.e., corrosion resistance) [27–30]. However, it remains a great challenge to confine high-valence metal single atoms within the lattice structure of Co-based LDHs and to efficiently activate their OER activity and stability through precise regulation and assembly.

In this work, we demonstrate a facile and effective strategy to assemble a confined single-atom W within the lattice of a CoFe-LDH electrocatalyst (CoFeW-LDH), which exhibits excellent OER activity and durability. The OER overpotentials at current densities (J) of 10 and 100 mA·cm^{-2} were determined to be 263 and 323 mV, respectively, far superior to those of bimetallic CoFe-LDH and Co-LDH and comparable to the commercial IrO_2 catalyst. Furthermore, it shows outstanding durability at a high current density of 1 A·cm^{-2} over 100 h in 1 M potassium hydroxide (KOH). The enhanced OER activity of CoFeW-LDH stems from the introduction of W, which induces the formation of extensive defects because of the significant difference in atomic radius and valence electron structure between Co and W, and triggers the local electronic reconfiguration of the adjacent Co sites around the defects, thereby delivering excellent catalytic OER performance.

2 Experimental

2.1 Chemicals and reagents

2-Methylimidazole (2-MeIM, $C_4H_6N_2$, 98.0%, Shanghai Macklin Biochemical Co., Ltd.), cetyltrimethyl ammonium bromide (CTAB, $C_{19}H_{42}BrN$, ≥ 99.0%, Shanghai Macklin Biochemical Co., Ltd.), ferrous sulfate heptahydrate ($FeSO_4·7H_2O$, 99.0%, Shanghai Macklin Biochemical Co., Ltd.), cobalt nitrate hexahydrate ($Co(NO_3)_2·6H_2O$, 99.0%, Tianjin Oubokai Chemical Co., Ltd.), tungsten chloride (WCl_6, 99.5%, Shanghai Energy Chemical Co., Ltd.), KOH (99.0%, Tianjin Kemiou Chemical Reagent Co., Ltd.), and ethanol (C_2H_5OH, ≥ 99%, Tianjin Zhiyuan Chemical Reagent Co., Ltd.) were used directly without further purification. Nafion solution (~ 5 wt.%, Sigma-Aldrich) was used as binder. All aqueous solutions were prepared using Milli-Q water (18.2 MΩ·cm, total organic carbon (TOC) of 5 ppm).

2.2 Synthesis of zeolitic-imidazolate frameworks-67 (ZIF-67)

First, 240 mg of $Co(NO_3)_2·6H_2O$ and 6 mg of $C_{19}H_{42}BrN$ were completely dissolved in 8 mL of water. This solution was then rapidly added into 56 mL of 3.632 g 2-MeIM-dissolved aqueous solution during stirring at room temperature. The reaction mixture was stirred for an additional 20 min. Afterward, the formed ZIF-67 was collected by centrifugation, washed with ethanol, and dried overnight at 60 °C.

2.3 Synthesis of CoFe-LDH, CoW-LDH, and CoFeW-LDH

The obtained ZIF-67 template was re-dispersed in 120 mL of ethanol, and then dropwise added into 50 mL of an aqueous solution containing a certain amount of $FeSO_4·7H_2O$, WCl_6, or both to achieve different molar ratios of Co:Fe, Co:W, or Co:Fe:W. The mixture was transferred to a round-bottom flask and heated to reflux at 85 °C for 2 h. The target product was collected by centrifugation, washed alternately with water and ethanol three times, and then dried for further use. The different molar ratios of Co, Fe, and W in the CoFe-LDH, CoW-LDH, and CoFeW-LDH were obtained by varying the molar concentrations of ZIF-67, $FeSO_4·7H_2O$, and WCl_6 in the precursor solution.

2.4 Structural characterizations

X-ray diffraction (XRD) measurement was conducted using a Bruker D8 ADVANCE diffractometer with a Cu Kα anode (λ = 1.5406 Å) operating at 40 kV and 40 mA (2θ = 5°–90°). Morphological structure characterizations were performed on a Zeiss Sigma 500 field emission scanning electron microscope (FE-SEM) operated at 10 kV, and a JEOL JEM-2100F high-resolution transmission electron microscope (HR-TEM) operated at an accelerating voltage of 200 kV, equipped with an Oxford Instruments X-MET8000 energy-dispersive X-ray spectrometer (EDS). Atomic-resolution scanning TEM (AC-STEM) images were acquired using a JEOL JEM-ARM300F microscope equipped with a probe-forming aberration corrector, operating at an accelerating voltage of 300 kV. Atomic force microscopy (AFM) measurements were performed on the Bruker Dimension Icon, and the data were processed using the NanoScope Analysis software. The surface chemical composition and valence state were examined by X-ray photoelectron spectroscopy (XPS) using a Thermo ESCALAB 250Xi spectrometer. All the binding energy positions were calibrated using the C 1s at 284.8 eV from adventitious carbon. Quantitative analysis of the metal elements was carried out by inductively coupled plasma optical emission spectrometry (ICP-OES). X-ray absorption spectroscopy (XAS) was conducted using a Rapid-XAFS 1M (Anhui Absorption Spectroscopy Analysis Instrument Co., Ltd.) in transmission mode at 25 kV and 40 mA. The test specimens were prepared by the KBr-disk method.

2.5 Electrochemical measurements

A three-electrode system, consisting of a catalyst-coated glassy carbon (GC) disk working electrode with a diameter of 5 mm, carbon rod counter electrode, and Hg/HgO reference electrode, which is equipped with an electrochemical workstation (CHI750E, CH Instruments, Inc.), was employed for electrochemical measurements. To prepare the catalyst-coated GC electrode, a

catalyst suspension was first prepared by ultrasonically dispersing 4 mg of catalyst, 4 mg of activated carbon, and 20 μL of a 5% Nafion solution in 1 mL of anhydrous ethanol. Subsequently, 25 μL of the catalyst suspension was spin-coated onto the GC working electrode and dried under an infrared lamp, resulting in a catalyst loading of ~ 500 μg·cm^{-2}. Linear sweep voltammetry (LSV) curves were recorded using the catalyst-coated GC rotating disk electrode (RDE) at a scan rate of 5 mV·s^{-1} and a rotation speed of 1600 rpm. All potentials in the LSVs were converted to the reversible hydrogen electrode (RHE) scale with *iR*-compensation. Tafel slopes were derived from the LSV data by plotting the logarithmic current density against the potential. Electrochemical impedance spectroscopy (EIS) measurements were performed in the frequency range from 100 kHz to 0.01 Hz at 1.5 V (vs. RHE). The electrochemically active surface area (ECSA) was proportional to the double-layer capacitance (C_{dl}), which was determined from the slope of the charging *J* versus scan rate in cyclic voltammetry (CV) measurements conducted in the non-Faradaic region [31, 32]. A 30 h durability test was performed in 1 M KOH at 1.6 V (vs. RHE), using a working electrode of carbon paper (1 cm × 1 cm) coated with $Co_1Fe_{0.5}W_{0.125}$-LDH (mass loading: 500 μg·cm^{-2}), which is denoted as $Co_1Fe_{0.5}W_{0.125}$-LDH/A. For the simulated industrial water electrolysis test, an electrolyzer was assembled with a 3 cm × 3 cm $Co_1Fe_{0.5}W_{0.125}$-LDH/Ni anode and a 3 cm × 3 cm 20% Pt/C/Ni cathode, separated by a Fumasep FAA-3-PK-130 anion-exchange membrane in 1 M KOH. The evaluation was performed by chronopotentiometry at a constant current density of 1 A·cm^{-2}. 1 M KOH electrolyte was continuously supplied to both the anode and cathode chambers of the electrolyzer. The produced hydrogen and oxygen, along with the electrolyte, underwent gas–liquid separation before the electrolyte was recirculated. To compensate for water consumption, deionized water was replenished daily into the external reservoir. Potentials were converted to the RHE scale using the following equation: E (vs. RHE) = E (vs. Hg/HgO) + E^{θ} (Hg/HgO) + 0.059pH, where E is the electrode potential, and E^{θ} is the standard electrode potential. In order to evaluate the Faradaic efficiency (η_F) of the OER, a Hoffman electrolysis apparatus was used to collect the produced H_2 and O_2 in separate gas collection tubes with volume scales. The detailed experimental procedure and calculation method have been described in our previous work [33].

2.6 *In-situ* electrochemical characterizations

In-situ electrochemical Raman spectroscopy was performed on a LabRAM HR 800 Raman spectrometer using a 532 nm laser at a power of about 0.3 mW. The measurements were carried out in a commercial Raman cell, which consisted of a polycrystalline Au working electrode with a diameter of 5 mm, an Ag/AgCl reference electrode (E (vs. RHE) = E (vs. Ag/AgCl) + E^{θ} (Ag/AgCl) + 0.059pH), and a Pt wire counter electrode. *In-situ* attenuated total reflectance surface enhanced infrared absorption spectroscopy (ATR-SEIRAS) measurements were conducted using a Bruker Vertex 70 V spectrometer equipped with a liquid nitrogen-cooled mercury cadmium telluride (MCT) detector and an IR optical accessory (SPEC-I, Shanghai Yuanfang Technology Co., Ltd.) with an optimized beam incidence angle of approximately 60° on the reflection plane of the working electrode. The IR spectra were acquired at a resolution of 8 cm^{-1}, with the time for each single-beam spectrum acquisition of 20 s. All spectra are presented in absorbance, defined as $-\log(R/R_0)$, where R and R_0 correspond to the sample and reference single-beam spectrum, respectively.

2.7 Density functional theory (DFT) calculations

Spin-polarized DFT calculations were performed using the Vienna *ab initio* simulation package (VASP, version 6.1.0). The electron exchange-correlation interactions were described using the generalized gradient approximation (GGA) with the Perdew–Burke–Ernzerhof (PBE) functional. Projector augmented wave (PAW) pseudopotentials were employed to model the ion-electron interactions. A plane-wave cutoff energy of 500 eV was adopted for the DFT calculations. Structural relaxations were carried out with stringent convergence criteria, requiring the residual forces on each atom to be less than 0.05 eV·Å^{-1} and the total energy differences between successive steps to be below 1 × 10^{-6} eV. A Monkhorst–Pack *k*-point grid of 2 × 2 × 1 was used to sample the Brillouin zone of the face-centered cubic lattice. In addition, a vacuum layer of 15 Å was applied along the *z*-direction to avoid spurious interactions between periodic images of the simulation cell.

3 Results and discussion

3.1 Physical characterization

ZIF-67-derived CoFeW-LDHs with a nanosheet-assembled hollow nanocube structure were synthesized via a solvothermal method, as illustrated in Scheme S1 in the Electronic Supplementary Material (ESM). Initially, ZIF-67 with a regular nanocube structure was successfully prepared as a sacrificial template (Fig. 1(a) and Fig. S1 in the ESM). The XRD pattern of ZIF-67 (Fig. S2 in the ESM) matches well with those reported in Refs. [34, 35]. Subsequently, ZIF-67-derived CoFe-LDH, CoW-LDH, and CoFeW-LDHs were synthesized, and their XRD patterns (Fig. S3 in the ESM) confirmed the successful formation of these LDHs. For $Co_1Fe_{0.5}W_{0.125}$-LDH, the negative shifts and broadened full width at half maximum (FWHM) of the characteristic (003), (006), and (012) diffraction peaks compared to the undoped $Co_1Fe_{0.5}$-LDH indicate the successful introduction of W. Morphological characterization (Figs. S4–S6 in the ESM) reveals that most of the multimetallic LDHs failed to maintain the nanocube morphology of the ZIF-67 template. This is attributed to the lattice mismatch induced by the incorporation of foreign metal atoms into the host Co-LDH lattice, leading to the aggregation of nanosheets and nanoparticles after structural collapse.

However, a portion of the $Co_1Fe_{0.5}W_{0.125}$-LDH samples before and after OER retained the nanosheets-assembled hollow nanocubic structure, as clearly evidenced by the HR-TEM (Fig. 1(b)) and high-angle annular dark-field (HAADF)-STEM (Fig. 1(e) and Figs. S6 and S7 in the ESM) images. The thickness of these nanosheets was measured by AFM to be approximately 5.5 nm (Fig. 1(c)). On the nanosheet surface, W and Fe single atoms are uniformly dispersed, as indicated by the well-distributed bright spots marked with red solid circles in Fig. 1(d). Intensity profiles taken along positions 1 to 4 in Fig. 1(d) unambiguously confirm that both Fe and W atoms are co-confined within the Co-LDH lattice. Additionally, numerous defects are visible in the basal plane (highlighted by green solid circles in Fig. 1(d)), which arise from the lattice misfit caused by differences in atomic radii (r_{Co} = 125 pm; r_{Fe} = 126 pm; and r_W = 137 pm) and intermetallic bond energies. It is generally recognized that the difference in atomic radii and bonding energy serves as the key driving force for the formation of lattice defects. Their synergistic effect directly leads to lattice mismatch and localized

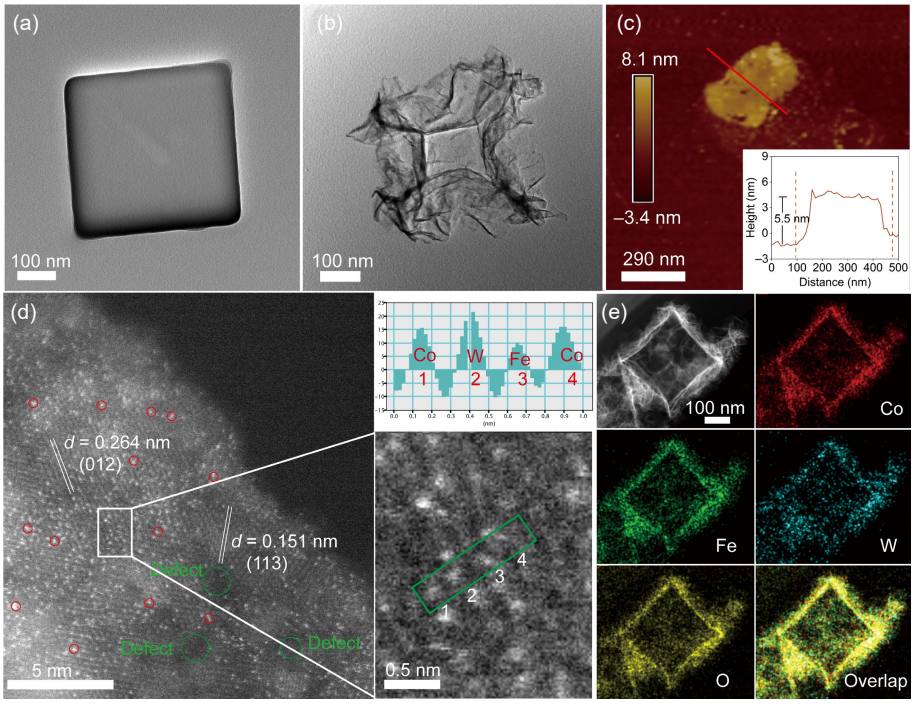

Figure 1 Morphology and structure characterizations. HR-TEM images of (a) ZIF-67 template and (b) $Co_1Fe_{0.5}W_{0.125}$-LDH. (c) AFM image of the $Co_1Fe_{0.5}W_{0.125}$-LDH nanosheet. (d) AC-STEM image of $Co_1Fe_{0.5}W_{0.125}$-LDH, where the red solid circles highlight individually dispersed W atoms and the green solid circles mark the defect sites. (e) The HAADF-STEM image and the corresponding EDS elemental mappings of $Co_1Fe_{0.5}W_{0.125}$-LDH.

stress fields, thereby inducing defects [36, 37]. These structural imperfections generate abundant unsaturated metal sites, which are expected to enhance catalytic performance. The AC-STEM images of $Co_1Fe_{0.5}W_{0.125}$-LDH (Fig. 1(d) and Fig. S8 in the ESM) clearly reveal the well-defined lattice fringes with interplanar distances of 0.264 and 0.151 nm, corresponding to the (012) and (113) planes, respectively. The (012) interplanar distance of $Co_1Fe_{0.5}W_{0.125}$-LDH (0.264 nm) is slightly larger than that of $Co_1Fe_{0.5}$-LDH (0.262 nm, Fig. S9 in the ESM), suggesting lattice expansion due to the incorporation of W atoms. EDS elemental mappings further confirm the homogeneous distribution of Co, Fe, W, and O throughout the $Co_1Fe_{0.5}W_{0.125}$-LDH nanosheet (Fig. 1(e) and Fig. S10 in the ESM).

XPS and XAS measurements were employed to determine the chemical compositions and electronic structures of the synthesized materials. The XPS spectra (Figs. 2(a)–2(c) and Figs. S11–S15 in the ESM) confirmed the presence of the expected elements in the target materials. In the Co 2p XPS spectra (Fig. 2(a) and Figs. S11 and S13–S15 in the ESM), the characteristic peaks at binding energies of 781.07 eV (Co^{3+} $2p_{3/2}$), 782.64 eV (Co^{2+} $2p_{3/2}$), 796.58 eV (Co^{3+} $2p_{1/2}$), and 798.22 eV (Co^{2+} $2p_{1/2}$) indicate the coexistence of Co^{2+} and Co^{3+} in these LDHs, which is consistent with previous reports [35, 38]. In contrast, ZIF-67 contains predominantly divalent cobalt (Co^{2+}), as shown in Fig. S12 in the ESM. As summarized in Table S1 in the ESM, the Co^{3+}/Co^{2+} peak area ratio for $Co_1Fe_{0.5}W_{0.125}$-LDH (1.06) is slightly lower than that for $Co_1Fe_{0.5}$-LDH (1.09), suggesting that the incorporation of W promotes the partial reduction of Co^{3+} to Co^{2+}. This finding is further supported by the slight negative shift in the Co K-edge X-ray absorption near-edge structure (XANES) spectrum of $Co_1Fe_{0.5}W_{0.125}$-LDH relative to $Co_1Fe_{0.5}$-LDH (Fig. 2(d)). A similar phenomenon, where Ir incorporation induced reduction of Co species in CoMo-LDH, has been reported previously [34]. In the Fe 2p XPS spectra (Fig. 2(b)), the peaks at 712.13 and 724.17 eV are assigned to Fe^{2+}, while those at 715.62 and 726.95 eV correspond to Fe^{3+} [39, 40]. As listed in Table S2 in the ESM, the incorporation of W also leads to the partial reduction of Fe^{3+} to Fe^{2+}, which is consistent with the negative shift observed in the Fe K-edge XANES spectrum of $Co_1Fe_{0.5}W_{0.125}$-LDH compared to the W-free $Co_1Fe_{0.5}$-LDH (Fig. 2(e)). For the W 4f XPS spectra (Fig. 2(c)), the peaks at 34.71 eV (W^{5+} $4f_{7/2}$), 35.49 eV (W^{6+} $4f_{7/2}$), 37.09 eV (W^{5+} $4f_{5/2}$), 37.68 eV (W^{6+} $4f_{5/2}$), and 40.87 eV (W^{6+} $5p_{3/2}$) are identified according to Refs. [41, 42]. Compared to $Co_1W_{0.5}$-LDH, both $Co_1Fe_{0.5}W_{0.125}$-LDH and $Co_1Fe_{0.5}W_{0.5}$-LDH exhibit larger W^{6+}/W^{5+} ratios (Table S3 in the ESM). The position of the W L_3-edge XANES spectrum for $Co_1Fe_{0.5}W_{0.125}$-LDH (Fig. 2(f)) between those of WO_3 and WO_2 further confirms the presence of W^{5+} species, which is probably associated with the formation of vacancies or defects [42]. The partial reduction of Co^{3+} and Fe^{3+} induced by W incorporation can be rationalized by the relative ionic electronegativity sequence of the metal centers, i.e., W^{6+} (1.67 eV) < Fe^{3+} (2.20 eV) < Co^{3+} (2.56 eV), and this suggests possible electron transfer from W to Fe and subsequently to Co [43]. In the S 2p XPS spectra (Figs. S11 and S14 in the ESM), the peaks at 168.36 and 169.57 eV for $Co_1Fe_{0.5}$-LDH and $Co_1Fe_{0.5}W_{0.125}$-LDH are related to S–O and SO_4^{2-} species, respectively [35]. The presence of S is probably due to the residual SO_4^{2-} from the sulfate precursor used during synthesis. For O 1s XPS spectra (Figs. S11 and S14 in the ESM), the peaks at 531.27 and 532.87 eV for $Co_1Fe_{0.5}$-LDH and $Co_1Fe_{0.5}W_{0.125}$-LDH are associated with M–OH (M = Co, Fe, and W) and S–O, respectively. However, the absence of the S–O signal in $Co_1W_{0.5}$-LDH, confirms that S originates from the ferrous sulfate used during synthesis process.

To elucidate the evolution of metal valence states during the OER process, we performed *ex-situ* XPS measurement on the $Co_1Fe_{0.5}W_{0.125}$-LDH/A catalyst before and after a 30 h OER stability test at 1.6 V (vs. RHE) in 1 M KOH (Fig. S23 in the ESM). The XPS

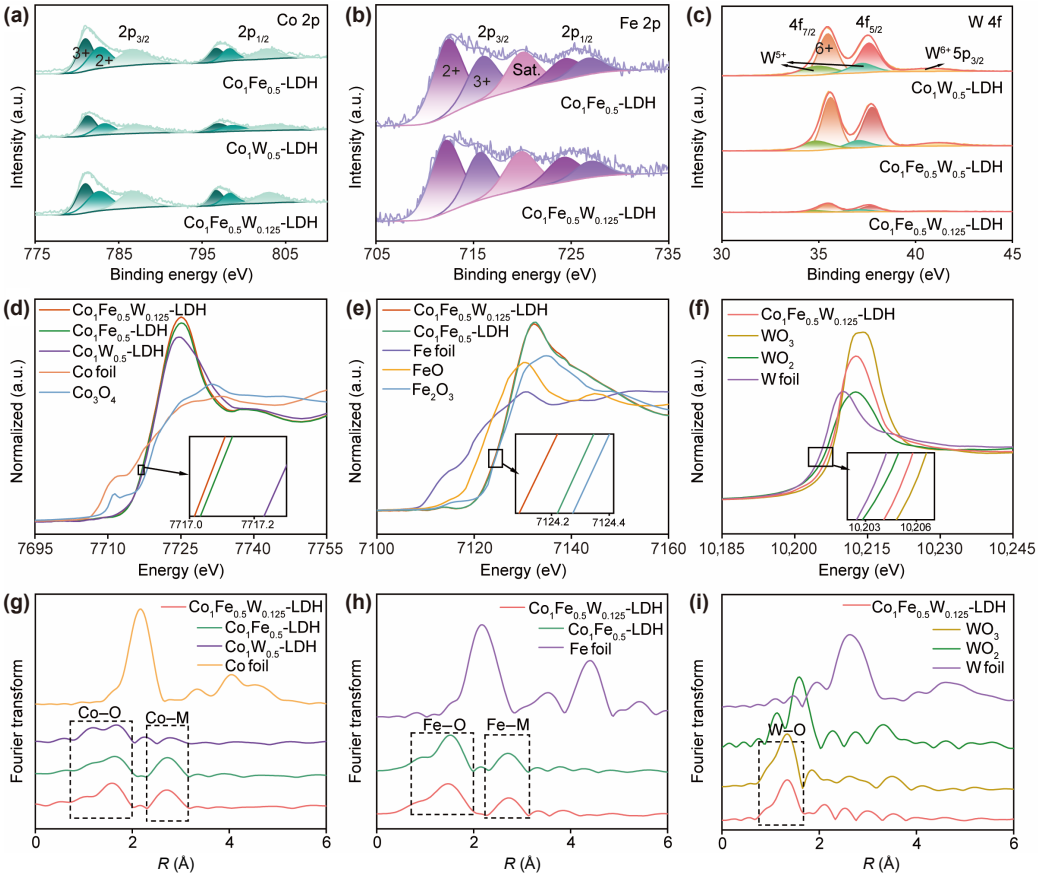

Figure 2 Electronic and coordination structure characterizations. High resolution XPS spectra of (a) Co 2p, (b) Fe 2p, and (c) W 4f. XANES spectra of (d) Co K-edge, (e) Fe K-edge, and (f) W L_3-edge. FT-EXAFS spectra of $Co_1Fe_{0.5}W_{0.125}$-LDH: (g) Co K-edge, (h) Fe K-edge, and (i) W L_3-edge.

spectra (Fig. S16 in the ESM) and quantitative analysis (Tables S1 and S2 in the ESM) reveal a significant increase in the relative proportions of Co^{3+} and Fe^{3+} species after the test. These results suggest the formation of higher oxidation-state metal sites, which are likely the catalytically active species for the OER.

The Fourier transform extended X-ray absorption fine structure (FT-EXAFS) spectra were analyzed to determine the local coordination environments, as shown in Figs. 2(g)–2(i). In the Co K-edge FT-EXAFS spectra (Fig. 2(g)), $Co_1Fe_{0.5}W_{0.125}$-LDH, $Co_1Fe_{0.5}$-LDH, and $Co_1W_{0.5}$-LDH show two prominent peaks at approximately 1.6 and 2.7 Å, corresponding to typical Co–O and Co–M (M = Co, Fe, or W) bonds, respectively. Notably, the incorporation of W causes a noticeable expansion in the second coordination shell (Co–M) and increases the number of defects, which can be explained by the larger covalent radius of W compared to Fe and Co. Moreover, the lower peak intensities of Co–M bond in $Co_1W_{0.5}$-LDH and $Co_1Fe_{0.5}W_{0.125}$-LDH compared to $Co_1Fe_{0.5}$-LDH (Fig. 2(g)) indicate that W incorporation induces local structural distortion around Co centers, consistent with the reduced crystallinity observed in the XRD patterns. As shown in Fig. 2(h), the Fe K-edge FT-EXAFS spectra display peaks at ~ 1.6 and 2.6 Å, assigned to the Fe–O and Fe–M (M = Co, Fe, or W), respectively. After incorporation of W, the Fe–O peak broadens slightly, and the shoulder that appeared at ~ 1.2 Å becomes less pronounced, suggesting a weakening of the Fe–O stretching vibration and the presence of defects. The W L_3-edge FT-EXAFS spectrum of $Co_1Fe_{0.5}W_{0.125}$-LDH (Fig. 2(i)) shows a dominant peak at ~ 1.3 Å, corresponding to the W–O, suggesting that W atoms are stabilized by the coordinative oxygen atoms due to the oxophilic property of W^{6+}. The *q* space transition of EXAFS spectra for W element in $Co_1Fe_{0.5}W_{0.125}$-LDH (Fig. S17 in the ESM) reveals a local coordination environment similar to that of W in WO_3. Compared with the W foil reference, the absence of a W–W metallic bond in $Co_1Fe_{0.5}W_{0.125}$-LDH confirms that W species are atomically dispersed within the LDH host, which is in agreement with the AC-STEM results. All these results verify the successful incorporation of W and Fe into the Co-LDH lattice via oxygen coordination, forming a typical (oxy)hydroxide octahedral structure. Additionally, the presence of abundant defects and the effective confinement of atomic W within the CoFe-LDH framework are also evident.

3.2 The electrocatalytic OER performance

The electrocatalytic OER performance was evaluated at room temperature using a standard three-electrode system in 1 M KOH solution. A glassy carbon RDE was used as the working electrode, where the catalyst was uniformly drop-coated at a constant mass loading of 0.50 mg·cm^{-2}. In our previous study, $Co_1Fe_{0.5}$-LDH was identified as a highly active catalyst following systematic optimization of Co and Fe ratios [35]. On this basis, we carefully investigated the effect of W incorporation on the OER activity of $Co_1Fe_{0.5}$-LDH in this work. As demonstrated in Figs. S18 and S19 in the ESM, the OER activity initially improves with increasing W content up to an optimal atomic ratio of 0.125, beyond which further W incorporation results in a decrease in catalytic performance. Therefore, the $Co_1Fe_{0.5}W_{0.125}$-LDH exhibits the highest OER catalytic activity, achieving remarkably low overpotentials of

263 and 323 mV at current densities of 10 and 100 mA·cm^{-2}, respectively. These values are significantly lower than those of the optimized bimetallic counterparts ($Co_1Fe_{0.5}$-LDH and $Co_1W_{0.5}$-LDH) and the pristine Co-LDH (ZIF-67) (Figs. 3(a) and 3(b) and Fig. S20 in the ESM). This enhanced catalytic activity can be attributed to the favorable local coordination environment and electronic structure of the active metal sites created by incorporating W and Fe into the Co-LDH lattice, which optimizes the reaction energetics for OER [44], thereby strengthening the synergistic effect among the metal centers and ultimately boosting OER performance. The Tafel slope of the $Co_1Fe_{0.5}W_{0.125}$-LDH was determined to be 35.8 mV·dec^{-1}, which is significantly smaller than those of other trimetallic CoFeW-LDHs, bimetallic $Co_1Fe_{0.5}$-/$Co_1W_{0.5}$-LDH, and the pristine Co-LDH (Fig. 3(c)), indicating more favorable OER kinetics. Notably, the performance of the as-prepared $Co_1Fe_{0.5}W_{0.125}$-LDH surpasses that of most state-of-the-art cobalt-based non-precious metal electrocatalysts reported in recent Refs. [45–52] (Fig. 3(d) and Table S4 in the ESM).

EIS measurements were conducted to further evaluate the interfacial charge transfer kinetics. The Nyquist plots and the equivalent circuit diagram are shown in Fig. 3(e), where R_s, R_{ct}, and CPE denote the solution resistance, charge-transfer resistance, and constant phase element, respectively. The values of R_s and R_{ct} are summarized in Table S5 in the ESM. These results reveal that $Co_1Fe_{0.5}W_{0.125}$-LDH exhibits the lower R_{ct} compared to others (Fig. 3(e) and Fig. S18(d) in the ESM), suggesting significantly accelerated charge transfer at the electrode–electrolyte interface during the OER. This reduced R_{ct} can be attributed to the optimized surface electronic structure resulting from the co-incorporation of Fe and W [53, 54]. Electrochemical surface area (ECSA) is a critical property to evaluate the electrocatalytic performance of catalysts. According to the equation of ECSA = C_{dl}/C_s, where C_s is the specific capacitance (25 μF·cm^{-2}), the value of ECSA is proportional to the C_{dl}, which was evaluated by measuring the capacitive current in a non-Faradaic potential window [31, 32, 35]. Cyclic voltammograms recorded at different scan rates are presented in Figs. S19 and S21 in the ESM. The C_{dl} values were determined from the slope of the current density difference ($\Delta J = (J_a - J_c)/2$, where J_a and J_c represent the anodic and cathodic current densities, respectively) versus scan rates. As shown in Fig. 3(f), $Co_1Fe_{0.5}W_{0.125}$-LDH exhibits the highest C_{dl} value (55.9 mF·cm^{-2}), reflecting the largest ECSA among the catalysts. In addition, the ECSA-normalized LSV curves for the OER are presented in Fig. S22 in the ESM, suggesting that $Co_1Fe_{0.5}W_{0.125}$-LDH also possesses excellent intrinsic activity. Based

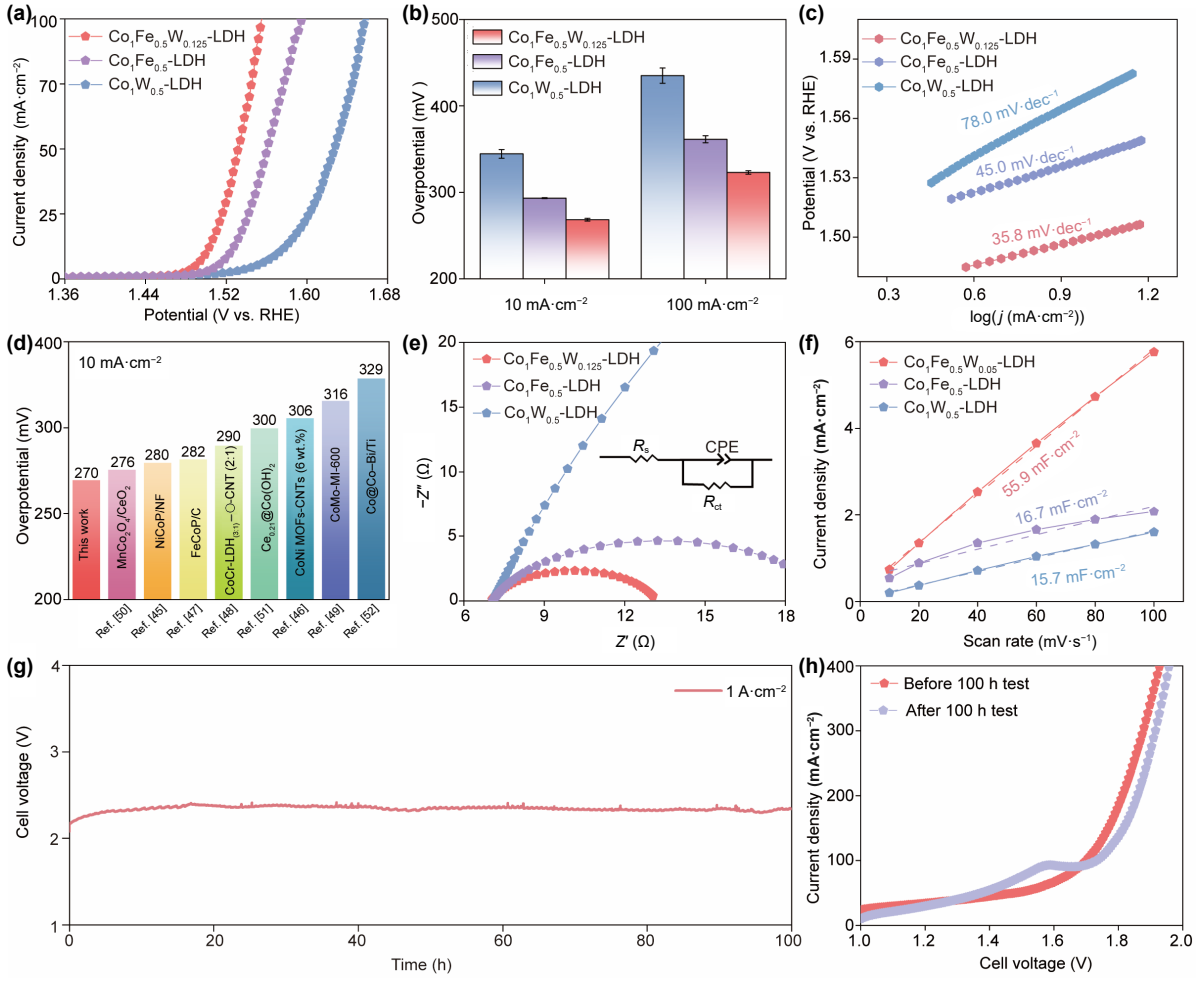

Figure 3 Electrocatalytic OER performance. (a) *iR*-corrected OER polarization curves of $Co_1Fe_{0.5}W_{0.125}$-LDH, $Co_1Fe_{0.5}$-LDH, and $Co_1W_{0.5}$-LDH in 1 M KOH at a scan rate of 5 mV·s^{-1}. (b) The corresponding overpotentials at 10 and 100 mA·cm^{-2}. (c) Tafel slopes derived from the LSVs (a). (d) Comparison of the overpotentials at 10 mA·cm^{-2} for the optimal catalyst ($Co_1Fe_{0.5}W_{0.125}$-LDH) with those of other cobalt-based non-noble metal electrocatalysts reported in the literatures (Table S4 in the ESM). (e) Nyquist plots from EIS measurements performed at a potential of 1.52 V (vs. RHE). (f) C_{dl} values for each catalyst. (g) Cell voltage measured during operation at the high current density of 1 A·cm^{-2} in an AWE. (h) Non-*iR*-corrected LSVs before and after 100 h stability test at high current density.

on the ICP-OES results (Table S6 in the ESM), the turnover frequency (TOF) value at the overpotential of 300 mV for the optimal $Co_1Fe_{0.5}W_{0.125}$-LDH catalyst was calculated to be 6.35 s^{-1}, which surpasses those of comparable catalysts listed in Table S7 in the ESM. The OER stability of $Co_1Fe_{0.5}W_{0.125}$-LDH was assessed by chronoamperometry at 1.60 V (vs. RHE). As shown in Fig. S23 in the ESM, the current–time (*I*–*t*) curve over 30 h displays an initial activation-induced increase followed by only marginal decay, with overall variation remaining within 5%. Excellent stability was further confirmed by comparing cyclic voltammetry scans before and after the test (Fig. S24 in the ESM), which show nearly overlapping polarization curves with negligible change.

For practical application in industrial electrolysis, a lab-scale alkaline water electrolyzer (AWE) [35] consisting of a $Co_1Fe_{0.5}W_{0.125}$-LDH/nickel foam (NF) anode and a commercial 20% Pt/C/NF cathode, separated by a Fumasep FAA-3-PK-130 anion-exchange membrane, was assembled. The performance was evaluated via chronopotentiometry at near-industrial current densities in a pump-circulated 1 M KOH solution at room temperature. The electrolyzer required an average cell voltage of only ~ 2.34 V to deliver a high current density of 1 A·cm^{-2} for over 100 h (Fig. 3(g)). Moreover, the near-complete overlap of LSV curves before and after the stability test (Fig. 3(h)) attests to excellent catalytic stability, which stems from optimized surface electronic structure and W-doping-enhanced structural stability, as verified by the structural integrity before and after OER via TEM images (Fig. 1(b) and Fig. S7 in the ESM). High-valence W^{6+} modulates the electron density of adjacent metal sites and introduces robust W–O and M–O bonds, thus stabilizing LDH structure and boosting its chemical stability in harsh environments. These results demonstrate the promising potential of $Co_1Fe_{0.5}W_{0.125}$-LDH@NF as a highly efficient OER electrocatalyst for practical industrial water electrolysis.

The Faradaic efficiency of OER was determined using a Hoffman electrolysis apparatus. The chronoamperometric response was monitored at ~ 1.50 V (with *iR*-correction, R_s = 120 Ω). The volumes of H_2 and O_2 produced at cathode and anode were collected in the corresponding gas sampling tubes, respectively, and recorded with an interval of every 2 h and repeated ten times (20 h in total), as shown in the upper part of Fig. S25 in the ESM. The η_F was calculated using the equation of η_F (%) = (Q_{O_2}/Q_{total}) × 100%, where Q_{O_2} represents the electric charge required for the amount of O_2 actually produced, and Q_{total} is the total electric charge passed during the electrochemical oxidation process. The corresponding volumes of H_2 and O_2, along with the calculated Faradaic efficiency at each stage, are presented in the middle and bottom parts of Fig. S25 in the ESM, respectively. The calculated η_F values at each stage consistently approach nearly 100%. These results demonstrate that $Co_1Fe_{0.5}W_{0.125}$-LDH exhibits considerable potential as a high-performance and cost-effective cobalt-based non-precious metal electrocatalyst for OER applications.

3.3 *In-situ* detection of the intermediates and the surface structure evolution

The potential-dependent formation of surface-active phase was monitored by *in-situ* Raman spectroscopy. As shown in Fig. 4(a), an obvious phase transition process was indicated by the spectra recorded in the potential range of 1.35–1.70 V (vs. RHE) with an increment of 50 mV. More specifically, at the open circuit potential, several overlapping peaks appear between 400 and 750 cm^{-1}, and the visible peaks appeared at approximately 520, 570, and 680 cm^{-1} can be assigned to the F_{2g} and A_{1g} phonon modes of spinel Co_3O_4 [55–57], and/or Co–O vibrations in $Co(OH)_2$ [58–60]. The peak at ~ 570 cm^{-1} has also been attributed to Co–O in defective or disordered metal-doped-Co_3O_4 [61], while the peak at ~ 680 cm^{-1} may be assigned to the symmetric stretching vibration mode (A_{1g} symmetry) of Co–O in Co_3O_4-oxygen vacancy (V_O) [62]. As the potential increases to 1.50 V, significant electrochemical-driven surface reconstruction and phase transition are observed. At 1.45 V, a distinct peak emerges at 430 cm^{-1}, while the peaks at 520 and 570 cm^{-1} gradually merge or are overshadowed by a new peak at 530 cm^{-1}, indicating the initiation of structural reconstruction. Consequently, two dominant peaks arise at ~ 430 and 530 cm^{-1} at 1.50 V, corresponding to Co–O bond in CoOOH and the *O–Co(IV) moiety, respectively [63–65], which are recognized as active phases for OER [65–67]. Furthermore, the intensities of these peaks increase significantly with further increases in potential. These results indicate that the catalyst surface undergoes electrochemical reconstruction into OER-active phases during, or even prior to OER.

In-situ attenuated total reflection surface-enhanced infrared absorption spectroscopy (*In-situ* ATR-SEIRAS) was employed to capture the adsorbed intermediates formed on the catalyst surface during OER. The *in-situ* ATR-SEIRAS spectra were acquired between 1.2 and 2.0 V with a 100 mV interval, as presented in Fig. 4(b). The peak located at 1230 cm^{-1} is ascribed to the signal of Si–O–Si from the Si prism [35, 68]. A weak peak observed at

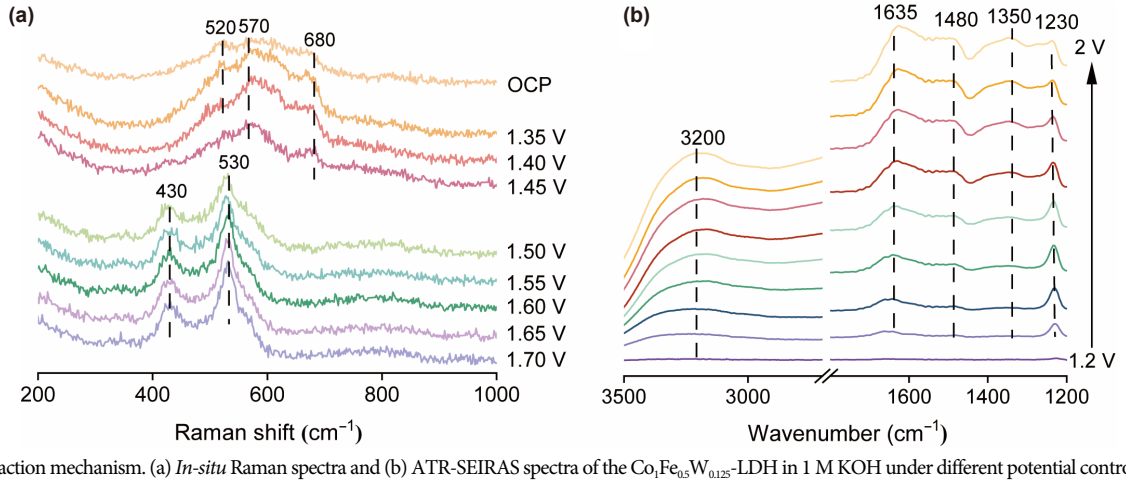

Figure 4 Reaction mechanism. (a) *In-situ* Raman spectra and (b) ATR-SEIRAS spectra of the $Co_1Fe_{0.5}W_{0.125}$-LDH in 1 M KOH under different potential controls.

~ 1350 cm^{-1} can be attributed to the O–O stretching vibration of adsorbed hydroperoxide species (OOH_{ad}), while the peak at ~ 1480 cm^{-1} is assigned to the O–O stretching vibration of weakly adsorbed molecular oxygen ($O_{2,ad}$), which is generated after deprotonation of OOH_{ad}. The peaks appearing at 1635 and 3200 cm^{-1} reflect the O–H bending and stretching modes of adsorbed hydroxyl species (OH_{ad}), respectively. As the applied potential increased to approximately 1.5 V, the emergence and accumulation of OOH_{ad} and $O_{2,ad}$ on the catalyst surface indicated the initiation of OER. It is consistent with the onset potential determined from the OER polarization curve. These findings provide valuable insights into the underlying mechanism of OER and activity enhancement mechanism.

3.4 DFT calculation

DFT calculations were performed on a series of structural models containing the in-plane-Co sites with unsaturated Co–O coordination, and structural-defect Co, Fe, and W sites (Fig. 5(a) and Fig. S26 in the ESM), to uncover the synergistic effect of the lattice-confined W single-atoms and their adjacent Fe and Co atoms on the OER activity. Initially, the activities of different metal sites in bimetallic CoFe- and CoW-LDH were compared to identify the component with relatively high activity and the corresponding active sites. It was found that CoFe-LDH exhibits higher catalytic activity, and the Co sites at defects were identified as the OER-active sites (Figs. S27 and S28 in the ESM). The rate-determining step (RDS) was determined to be the formation of *OOH intermediate, accompanied by the third electron transfer. For the trimetallic CoFeW-LDH, the Co sites at defects also serve as the more active centers (Fig. 5(d)). Notably, these Co sites in CoFeW-LDH show a lower limiting potential (0.37 eV) than those in the optimized bimetallic CoFe-LDH (0.54 eV) (Fig. 5(e)), suggesting that the incorporation of W effectively enhances the OER activity of adjacent Co sites. Moreover, the rate-determining step shifts to the release of the *OOH intermediates to subsequently form O_2 at the Co sites in the trimetallic CoFeW-LDH. Furthermore, the limiting potential for in-plane Co sites was calculated to be 1.53 eV, which is significantly higher than that of Co sites at defects (0.37 eV) (Fig. 5(e)). This significant difference is primarily attributed to the two distinct defect types, which exhibit fundamental differences in terms of unsaturated Co–O coordination environments and

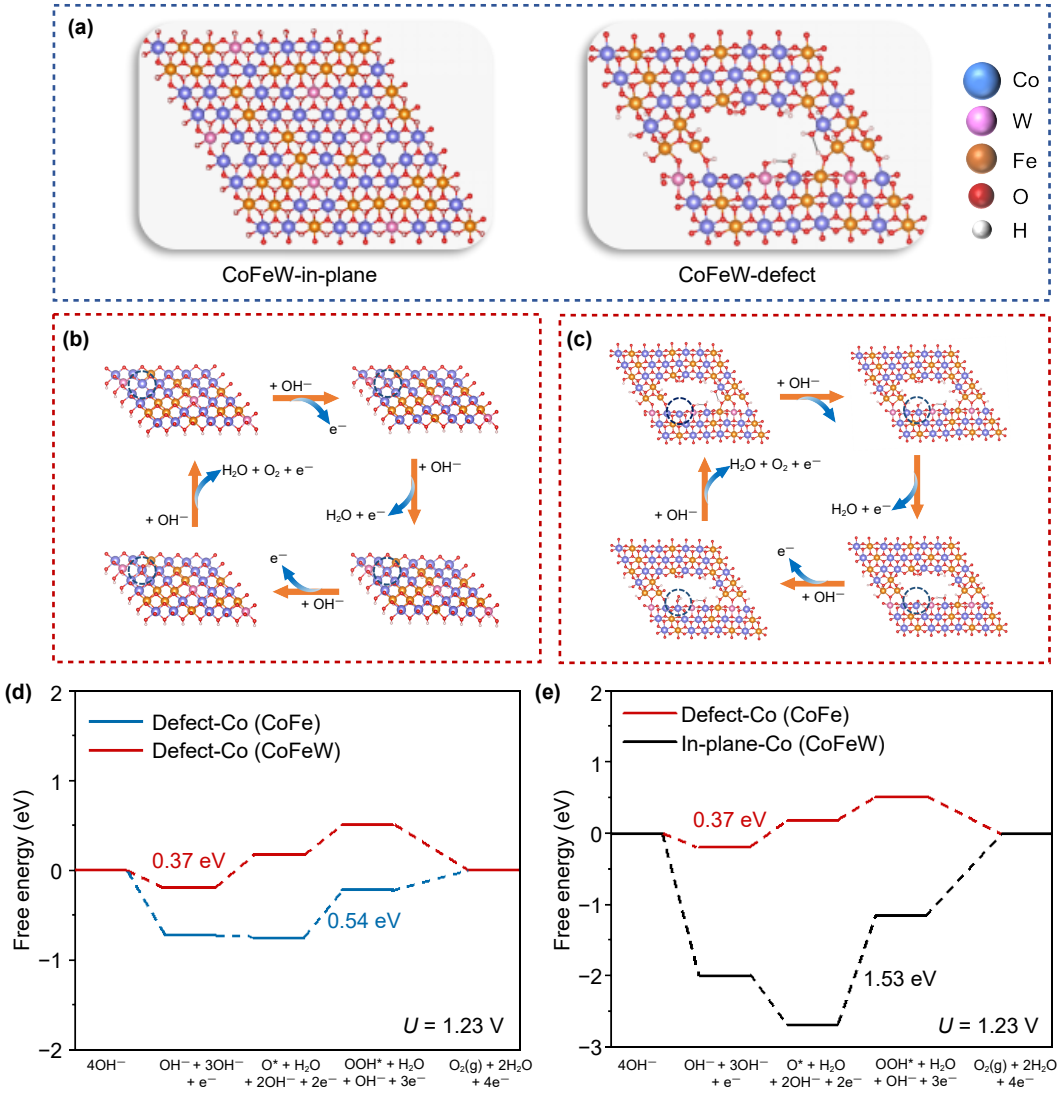

Figure 5 DFT calculations. (a) Structure models of CoFeW-LDH with a pristine surface (left) and a defect-containing surface (right). Atomic structures of OER intermediates adsorbed (b) at Co sites in the basal plane and (c) at the defects of CoFeW-LDH. (d) Gibbs free energy profiles for OER pathway at Co sites on CoFe-LDH, CoW-LDH, and CoFeW-LDH at 1.23 V. (e) Gibbs free energy profiles for OER pathway at the Co sites in the basal plane and at the defects at 1.23 V.

inherent structural defect characteristics, respectively. These results indicate that the W-adjacent, coordination-unsaturated Co sites located at defects and edges exhibit the highest OER activity. The corresponding adsorption structures of the reactants and intermediates are shown in Figs. 5(b) and 5(c). Overall, the DFT calculations suggest a catalytic activity trend of CoFeW-LDH > CoFe-LDH > CoW-LDH, which aligns well with the experimental results as shown in Fig. 3. The incorporation of W not only promotes the formation of numerous defects due to the differences in bonding energies between W–W and W–M bonds, as well as the differences in the atomic radii of Co, Fe, and W, but also modulates the electronic structure of adjacent metal atoms, thereby endowing CoFeW-LDH with superior OER catalytic performance.

4 Conclusions

In summary, a hollow cubic structured CoFeW-LDH assembled from ultrathin nanosheets with evenly distributed defects and the lattice-confined W single atoms was successfully synthesized via a facile solvothermal method. Benefiting from surface electronic reconfiguration and optimization, as well as the unique hollow nanocubic architecture, the CoFeW-LDH exhibits superior OER activity with a low Tafel slope of 35.8 $mV \cdot dec^{-1}$ and a low overpotential of merely 263 mV at 10 $mA \cdot cm^{-2}$, significantly outperforming most reported analogs. Moreover, it demonstrates outstanding durability over 100 h at 1 $A \cdot cm^{-2}$ in alkaline solution. DFT calculations reveal that the W-induced electronic reconfiguration of Co sites near defects enhances the catalytic activity by facilitating OER kinetics and charge transfer. This work provides a reliable strategy for designing lattice-confined high-valence metal single-atom catalysts with high atomic utilization and superior performance, presenting promising potential for applications in electrochemical energy storage and conversion.

Electronic Supplementary Material: Supplementary material is available in the online version of this article at https://doi.org/10.26599/NR.2026.94908561.

Data availability

All data needed to support the conclusions in the paper are presented in the manuscript and the Electronic Supplementary Material. Additional data related to this paper may be requested from the corresponding author upon request.

Acknowledgements

This work was financially supported by the National Natural Science Foundation of China (No. 22162026), the Sanqin Youth Talent Project of Shaanxi Province (No. YJ002), the Shaanxi Provincial Science and Technology Plan Project (Nos. 2020JQ-792 and 2025CY-YBXM-177), the Natural Science Basic Research Program of Shaanxi Province (No. 2024JCYBQN0118), the Science and Technology Plan Project of Yulin Government (Nos. 2023-CXY-213 and CXY-2022-186), and the Innovation and Entrepreneurship Training Program for Undergraduates (No. 202510719065).

Declaration of competing interest

All the contributing authors report no conflict of interests in this work.

Author contribution statement

L. X. Z.: Writing – review & editing, supervision, funding acquisition. L. L.: Writing – original draft, investigation. X. R. W.: Investigation. T. Y.: Methodology, investigation. K. T.: Investigation. H. L. Z.: Methodology, investigation. X. H. C.: Investigation. D. L. W.: Investigation. Y. C. T.: Investigation, writing – review & editing. J. L.: Methodology, writing – review & editing. X. B.: Writing – review & editing. W. L. Z.: Conceptualization, investigation. Q. B. W.: Writing – review & editing, supervision. F. F.: Writing – review & editing, funding acquisition. All the authors have approved the final manuscript.

Use of AI statement

None.

References

[1] Dawood, F.; Anda, M.; Shafiullah, G. M. Hydrogen production for energy: An overview. *Int. J. Hydrogen Energy* **2020**, *45*, 3847–3869.
[2] Dincer, I.; Acar, C. Review and evaluation of hydrogen production methods for better sustainability. *Int. J. Hydrogen Energy* **2015**, *40*, 11094–11111.
[3] Turner, J. A. Sustainable hydrogen production. *Science* **2004**, *305*, 972–974.
[4] Song, J. J.; Wei, C.; Huang, Z. F.; Liu, C. T.; Zeng, L.; Wang, X.; Xu, Z. C. J. A review on fundamentals for designing oxygen evolution electrocatalysts. *Chem. Soc. Rev.* **2020**, *49*, 2196–2214.
[5] Seitz, L. C.; Dickens, C. F.; Nishio, K.; Hikita, Y.; Montoya, J.; Doyle, A.; Kirk, C.; Vojvodic, A.; Hwang, H. Y.; Norskov, J. K. et al. A highly active and stable $IrO_x/SrIrO_3$ catalyst for the oxygen evolution reaction. *Science* **2016**, *353*, 1011–1014.
[6] Suntivich, J.; May, K. J.; Gasteiger, H. A.; Goodenough, J. B.; Shao-Horn, Y. A perovskite oxide optimized for oxygen evolution catalysis from molecular orbital principles. *Science* **2011**, *334*, 1383–1385.
[7] Xie, X. H.; Du, L.; Yan, L. T.; Park, S.; Qiu, Y.; Sokolowski, J.; Wang, W.; Shao, Y. Y. Oxygen evolution reaction in alkaline environment: Material challenges and solutions. *Adv. Funct. Mater.* **2022**, *32*, 2110036.
[8] McCrory, C. C. L.; Jung, S.; Ferrer, I. M.; Chatman, S. M.; Peters, J. C.; Jaramillo, T. F. Benchmarking hydrogen evolving reaction and oxygen evolving reaction electrocatalysts for solar water splitting devices. *J. Am. Chem. Soc.* **2015**, *137*, 4347–4357.
[9] Gozzo, C. B.; Soares, M. R. S.; Destro, F. B.; Junior, J. B. S.; Leite, E. R. Facile deposition of NiFe-LDH ultrathin film on pyrolytic graphite sheet for oxygen evolution reaction in alkaline electrolyte. *Int. J. Hydrogen Energy* **2022**, *47*, 8786–8798.
[10] Li, M. F.; Duanmu, K. N.; Wan, C. Z.; Cheng, T.; Zhang, L.; Dai, S.; Chen, W. X.; Zhao, Z. P.; Li, P.; Fei, H. L. Single-atom tailoring of platinum nanocatalysts for high-performance multifunctional electrocatalysis. *Nat. Catal.* **2019**, *2*, 495–503.
[11] Zhang, L.; Doyle-Davis, K.; Sun. X. L. Pt-based electrocatalysts with high atom utilization efficiency: From nanostructures to single atoms. *Energy Environ. Sci.* **2019**, *12*, 492–517.
[12] Yang, X. F.; Wang, A. Q.; Qiao, B. T.; Li, J.; Liu, J. Y.; Zhang, T. Single-atom catalysts: A new frontier in heterogeneous catalysis. *Acc. Chem. Res.* **2013**, *46*, 1740–1748.
[13] Lu, S. S.; Zhang, Z. P.; Cheng, C. Q.; Zhang, B.; Shi, Y. M. Unveiling the aggregation of M–N–C single atoms into highly efficient MOOH nanoclusters during alkaline water oxidation. *Angew. Chem., Int. Ed.* **2025**, *64*, e202413308.
[14] Yin, P. Q.; Yao, T.; Wu, Y. E.; Zheng, L. R.; Lin, Y.; Liu, W.; Ju, H. X.; Zhu, J. F.; Hong, X.; Deng, Z. X. et al. Single cobalt atoms with precise N-coordination as superior oxygen reduction reaction catalysts. *Angew. Chem., Int. Ed.* **2016**, *55*, 10800–10805.

[15] Chen, Y. J.; Ji, S. F.; Chen, C.; Peng, Q.; Wang, D. S.; Li, Y. D. Single-atom catalysts: Synthetic strategies and electrochemical applications. *Joule* **2018**, *2*, 1242–1264.
[16] Yu, Z. N.; Zhang, S. X.; Zhang, L. L.; Liu, X. Y.; Jia, Z. H.; Li, L.; Ta, N.; Wang, A.; Liu, W.; Wang, A. Q. et al. Suppressing metal leaching and sintering in hydroformylation reaction by modulating the coordination of Rh single atoms with reactants. *J. Am. Chem. Soc.* **2024**, *146*, 11955–11967.
[17] Yang, J. Y.; Huang, Y. K.; Qi, H. F.; Zeng, C. B.; Jiang, Q. K.; Cui, Y. T.; Su, Y.; Du, X. R.; Pan, X. L.; Liu, X. Y. et al. Modulating the strong metal–support interaction of single-atom catalysts via vicinal structure decoration. *Nat. Commun.* **2022**, *13*, 4244.
[18] Gu, J.; Jian, M. Z.; Huang, L.; Sun, Z. H.; Li, A. W.; Pan, Y.; Yang, J. Z.; Wen, W.; Zhou, W.; Lin, Y. et al. Synergizing metal–support interactions and spatial confinement boosts dynamics of atomic nickel for hydrogenations. *Nat. Nanotechnol.* **2021**, *16*, 1141–1149.
[19] Qin, R. X.; Liu, K. L.; Wu, Q. Y.; Zheng, N. F. Surface coordination chemistry of atomically dispersed metal catalysts. *Chem. Rev.* **2020**, *120*, 11810–11899.
[20] Fan, K.; Li, Z. H.; Song, Y. J.; Xie, W. F.; Shao, M. F.; Wei, M. Confinement synthesis based on layered double hydroxides: A new strategy to construct single-atom-containing integrated electrodes. *Adv. Funct. Mater.* **2021**, *31*, 2008064.
[21] Li, D. D.; Ding, L.; Zhang, S. H.; Zhang, P. F.; Prestigiacomo, C.; Wang, D. G.; Zhao, Q. *In-situ* electrostatic anchoring of highly oxidized Ir single atoms on NiFe LDH for efficient water oxidation. *Chem. Eng. J.* **2025**, *519*, 165662.
[22] Huo, J. M.; Ma, Z. L.; Wang, Y.; Cao, Y. J.; Jiang, Y. C.; Li, S. N.; Chen, Y.; Hu, M. C.; Zhai, Q. G. Monodispersed Pt sites supported on NiFe-LDH from synchronous anchoring and reduction for high efficiency overall water splitting. *Small* **2023**, *19*, 2207044.
[23] Ren, Y. F.; Wang, J. C.; Yang, L.; Gao, Q. F.; Li, P. P.; Zhang, Y.; Xiong, Y. C.; Fan, Z. X.; Quan, X.; Liu, Y. B. Single-atom Cu and Zn vacancy synergy in NiFe-LDH boosts metal–support interaction for high-efficiency nitrate-to-ammonia electroreduction. *Environ. Sci. Technol.* **2025**, *59*, 11414–11425.
[24] Gusmão, R.; Veselý, M.; Sofer, Z. Recent developments on the single atom supported at 2D materials beyond graphene as catalysts. *ACS Catal.* **2020**, *10*, 9634–9648.
[25] Zhao, S. Y.; Chen, G. X.; Zhou, G. M.; Yin, L. C.; Veder, J. P.; Johannessen, B.; Saunders, M.; Yang, S. Z.; De Marco, R.; Liu, C. et al. A universal seeding strategy to synthesize single atom catalysts on 2D materials for electrocatalytic applications. *Adv. Funct. Mater.* **2020**, *30*, 1906157.
[26] Yan, C.; Liu, Y. L.; Zeng, Q. Y.; Wang, G. G.; Han, J. C. 2D nanomaterial supported single-metal atoms for heterogeneous photo/electrocatalysis. *Adv. Funct. Mater.* **2023**, *33*, 2210837.
[27] Wang, H.; Zhai, T. T.; Wu, Y. F.; Zhou, T.; Zhou, B. B.; Shang, C. X.; Guo, Z. X. High-valence oxides for high performance oxygen evolution electrocatalysis. *Adv. Sci.* **2023**, *10*, 2301706.
[28] Li, L.; Cao, X. J.; Huo, J. J.; Qu, J. P.; Chen, W. H.; Liu, C. T.; Zhao, Y. F.; Liu, H.; Wang, G. X. High valence metals engineering strategies of Fe/Co/Ni-based catalysts for boosted OER electrocatalysis. *J. Energy Chem.* **2023**, *76*, 195–213.
[29] Deng, L. M.; Hung, S. F.; Lin, Z. Y.; Zhang, Y.; Zhang, C. C.; Hao, Y. X.; Liu, S. Y.; Kuo, C. H.; Chen, H. Y.; Peng, J. et al. Valence oscillation of Ru active sites for efficient and robust acidic water oxidation. *Adv. Mater.* **2023**, *35*, 2305939.
[30] Zhang, B.; Wang, L.; Cao, Z.; Kozlov, S. M.; De Arquer, F. P. G.; Dinh, C. T.; Li. J.; Wang. Z. Y.; Zheng, X. L.; Zhang. L. S. et al. High-valence metals improve oxygen evolution reaction performance by modulating 3d metal oxidation cycle energetics. *Nat. Catal.* **2020**, *3*, 985–992.
[31] Bo, X.; Hocking, R. K.; Zhou, S.; Li, Y. B.; Chen, X. J.; Zhuang, J. C.; Du, Y.; Zhao, C. Capturing the active sites of multimetallic (oxy)hydroxides for the oxygen evolution reaction. *Energy Environ. Sci.* **2020**, *13*, 4225–4237.
[32] McCrory, C. C. L.; Jung, S.; Peters, J. C.; Jaramillo, T. F. Benchmarking heterogeneous electrocatalysts for the oxygen evolution reaction. *J. Am. Chem. Soc.* **2013**, *135*, 16977–16987.
[33] Zhu, D.; Zan, L. X.; Tu, Y. C.; Zhang, W. L.; Zhang, H. L.; Luo, Y. X.; Liu, L.; Zheng, J. W.; Weng, Q.; Wei, Q. B. et al. Disclosing the intrinsic electrocatalytic activity of transition-metal sulfides for enhanced water oxidation. *Sci. China Chem.* **2025**, *68*, 4441–4449.
[34] Jia, R. N.; Xia, M. H.; Tang, L.; Yu, L.; Yang, Y.; Zhang, Y. L.; Bo, X.; Zhou, S. Z.; Tu, Y. C.; Deng, D. H. Single-atomic Ir and Mo co-confined in a Co layered hydroxide nanobox mutually boost oxygen evolution. *ACS Catal.* **2022**, *12*, 13513–13522.
[35] Liu, L.; Zan, L. X.; Tu, Y. C.; Zhang, H. L.; Zhu, D.; Li, Z.; Zheng, J. W.; Zhang, Z. Z.; Sun, Y.; Weng, Q. et al. Valence electronic engineering of hollow-nanocube-structured CoFeNi-layered double hydroxides for highly efficient oxygen evolution. *Chem. Eng. J.* **2024**, *500*, 156764.
[36] Budevski, E.; Staikov, G.; Lorenz, W. J. *Electrochemical Phase Formation and Growth: An Introduction to the Initial Stages of Metal Deposition*; Wiley-VCH: Weinheim, 1996.
[37] Gao, G. C.; Li, G. S.; Huang, T. T.; Wan, J. W.; Geng, Z. B.; Tang, H. T.; Zhao, X.; Fu, S. L.; Sun, L. Y.; Li, J. et al. Overcoming the activity–stability trade-off in electrocatalysts via unconventional two-step structural reconstructions of amorphous oxides. *J. Am. Chem. Soc.* **2025**, *147*, 29767–29778.
[38] Zhang, X. H.; Wu, A. P.; Wang, D. X.; Jiao, Y. Q.; Yan, H. J.; Jin, C. X.; Xie, Y.; Tian, C. G. Fine-tune the electronic structure in Co–Mo based catalysts to give easily coupled HER and OER catalysts for effective water splitting. *Appl. Catal. B Environ.* **2023**, *328*, 122474.
[39] Li, S. Y.; Song, X. S.; Kuai, X. X.; Zhu, W. C.; Tian, K.; Li, X. F.; Chen, M. Z.; Chou, S. L.; Zhao, J. Q.; Gao, L. J. A nanoarchitectured $Na_6Fe_5(SO_4)_8$/CNTs cathode for building a low-cost 3.6 V sodium-ion full battery with superior sodium storage. *J. Mater. Chem. A* **2019**, *7*, 14656–14669.
[40] Lu, Z.; Wang, J. K.; Zhang, P. F.; Guo, W. H.; Shen, Y. Q.; Liu, P. Z.; Ji, J. L.; Du, H. Y.; Zhao, M.; Liang, H. J. et al. Directed electron transport induced surface reconstruction of 2D NiFe-LDH/stanene heterojunction catalysts for efficient oxygen evolution. *Appl. Catal. B: Environ. Energy* **2024**, *353*, 124073.
[41] Dollinger, A.; Strobel, C. H.; Bleuel, H.; Seo, H. O.; Park, E. J.; Kim, Y. D.; Ganteför, G. Soft-landing of size-selected W clusters on highly ordered pyrolytic graphite surfaces: Towards the fabrication of thin films of cluster assemblies. *Curr. Appl. Phys.* **2015**, *15*, 1095–1099.
[42] Pandit, A.; Islam, M. M. Highly efficient bimetallic counter cations-based tungsten bronzes electrocatalysts developed for sustainable oxygen evolution in acidic solution. *Int. J. Hydrogen Energy* **2024**, *91*, 228–242.
[43] Sanderson, R. T. Electronegativity and bonding of transitional elements. *Inorg. Chem.* **1986**, *25*, 3518–3522.
[44] Zhang, B.; Zheng, X. L.; Voznyy, O.; Comin, R.; Bajdich, M.; García-Melchor, M.; Han, L. L.; Xu, J. X.; Liu, M.; Zheng, L. R. et al. Homogeneously dispersed multimetal oxygen-evolving catalysts. *Science* **2016**, *352*, 333–337.
[45] Liang, H. F.; Gandi, A. N.; Anjum, D. H.; Wang, X. B.; Schwingenschlögl, U.; Alshareef, H. N. Plasma-assisted synthesis of NiCoP for efficient overall water splitting. *Nano Lett.* **2016**, *16*, 7718–7725.
[46] Yu, S.; Wu, Y.; Xue, Q.; Zhu, J. J.; Zhou, Y. Z. A novel multi-walled carbon nanotube-coupled CoNi MOF composite enhances the oxygen evolution reaction through synergistic effects. *J. Mater. Chem. A* **2022**, *10*, 4936–4943.
[47] Zhao, R. G.; Ni, B. X.; Wu, L. M.; Sun, P. C.; Chen, T. H. Carbon-based iron-cobalt phosphate FeCoP/C as an effective ORR/OER/HER trifunctional electrocatalyst. *Colloids Surf. A: Physicochem. Eng. Asp.* **2022**, *635*, 128118.
[48] Malik, B.; Sadhanala, H. K.; Aziz, S. K. T.; Majumder, S.; Konar, R.; Gedanken, A.; Nessim, G. D. Synergy between cobalt-chromium-

layered double hydroxide nanosheets and oxidized carbon nanotubes for electrocatalytic oxygen evolution. *ACS Appl. Nano Mater.* **2022**, *5*, 4091–4101.

[49] Guo, Y. Y.; Huang, Q.; Ding, J. Y.; Zhong, L.; Li, T. T.; Pan, J. Q.; Hu, Y.; Qian, J. J.; Huang, S. M. CoMo carbide/nitride from bimetallic MOF precursors for enhanced OER performance. *Int. J. Hydrogen Energy* **2021**, *46*, 22268–22276.

[50] Fan, C.; Wu, X. D.; Li, M.; Wang, X.; Zhu, Y.; Fu, G. T.; Ma, T. Y.; Tang, Y. W. Surface chemical reconstruction of hierarchical hollow inverse-spinel manganese cobalt oxide boosting oxygen evolution reaction. *Chem. Eng. J.* **2022**, *431*, 133829.

[51] Zhou, Y. N.; Fan, R. Y.; Dou, S. Y.; Dong, B.; Ma, Y.; Yu, W. L.; Li, M. X.; Zhou, Y. L.; Liu, C. G.; Chai, Y. M. Tailoring electron transfer with Ce integration in ultrathin $Co(OH)_2$ nanosheets by fast microwave for oxygen evolution reaction. *J. Energy Chem.* **2021**, *59*, 299–305.

[52] Xie, C.; Wang, Y. Y.; Yan, D. F.; Tao, L.; Wang, S. Y. *In-situ* growth of cobalt@cobalt-borate core–shell nanosheets as highly-efficient electrocatalysts for oxygen evolution reaction in alkaline/neutral medium. *Nanoscale* **2017**, *9*, 16059–16065.

[53] Huang, J. W.; Sun, Y. H.; Zhang, Y. D.; Zou, G. F.; Yan, C. Y.; Cong, S.; Lei, T. Y.; Dai, X.; Guo, J.; Lu, R. F. et al. A new member of electrocatalysts based on nickel metaphosphate nanocrystals for efficient water oxidation. *Adv. Mater.* **2018**, *30*, 1705045.

[54] Yu, X. Y.; Feng, Y.; Jeon, Y.; Guan, B. Y.; Lou, X. W.; Paik, U. Formation of Ni–Co–MoS_2 nanoboxes with enhanced electrocatalytic activity for hydrogen evolution. *Adv. Mater.* **2016**, *28*, 9006–9011.

[55] Huang, J. Z.; Sheng, H. Y.; Ross, R. D.; Han, J. C.; Wang, X. J.; Song, B.; Jin, S. Modifying redox properties and local bonding of Co_3O_4 by CeO_2 enhances oxygen evolution catalysis in acid. *Nat. Commun.* **2021**, *12*, 3036.

[56] Silpa, S.; Mariyam, N.; Sharu, K.; Majumder, S.; Mitra, J.; Kamble, V. B. Novel $CuCo_2O_4$ photonic crystals for optical hydrogen sensing: Catalyst-free detection and mechanistic insights via *in-situ* Raman spectroscopy. *J. Mater. Chem. A* **2025**, *13*, 15016–15030.

[57] Chen, X.; Cai, S. C.; Yu, E. Q.; Li, J. J.; Chen, J.; Jia, H. P. Photothermocatalytic performance of ACo_2O_4 type spinel with light-enhanced mobilizable active oxygen species for toluene oxidation. *Appl. Surf. Sci.* **2019**, *484*, 479–488.

[58] Jing, C.; Yuan, T. T.; Li, L. L.; Li, J. F.; Qian, Z. X.; Zhou, J.; Wang, Y. F.; Xi, S. B.; Zhang, N.; Lin, H. J. et al. Electrocatalyst with dynamic formation of the dual-active site from the dual pathway observed by *in-situ* Raman spectroscopy. *ACS Catal.* **2022**, *12*, 10276–10284.

[59] Gao, P.; Zeng, Y.; Tang, P.; Wang, Z. X.; Yang, J. F.; Hu, A. P.; Liu, J. L. Understanding the synergistic effects and structural evolution of $Co(OH)_2$ and Co_3O_4 toward boosting electrochemical charge storage. *Adv. Funct. Mater.* **2022**, *32*, 2108644.

[60] Yang, J.; Liu, H. W.; Martens, W. N.; Frost, R. L. Synthesis and characterization of cobalt hydroxide, cobalt oxyhydroxide, and cobalt oxide nanodiscs. *J. Phys. Chem. C* **2010**, *114*, 111–119.

[61] Li, T.; Wang, Z. J.; Wang, L. H.; Wang, M. Y.; Liu, Y. Q. Nd and Ni Co-doped spinel Co_3O_4 nanosheet as an effective electrocatalyst for oxygen evolution reaction. *Appl. Catal. B: Environ. Energy* **2024**, *352*, 123990.

[62] Zhang, R. R.; Pan, L.; Guo, B. B.; Huang, Z. F.; Chen, Z. X.; Wang, L.; Zhang, X. W.; Guo, Z. Y.; Xu, W.; Loh, K. P. et al. Tracking the role of defect types in Co_3O_4 structural evolution and active motifs during oxygen evolution reaction. *J. Am. Chem. Soc.* **2023**, *145*, 2271–2281.

[63] Jia, H. N.; Yao, N.; Liao, Z. C.; Wu, L. Q.; Zhu, J.; Lao, Y. H.; Luo, W. Understanding the role of spin state in cobalt oxyhydroxides for water oxidation. *Angew. Chem., Int. Ed.* **2024**, *63*, e202408005.

[64] Yeo, B. S.; Bell, A. T. Enhanced activity of gold-supported cobalt oxide for the electrochemical evolution of oxygen. *J. Am. Chem. Soc.* **2011**, *133*, 5587–5593.

[65] Lee, W. H.; Han, M. H.; Ko, Y. J.; Min, B. K.; Chae, K. H.; Oh, H. S. Electrode reconstruction strategy for oxygen evolution reaction: Maintaining Fe–CoOOH phase with intermediate-spin state during electrolysis. *Nat. Commun.* **2022**, *13*, 605.

[66] Bergmann, A.; Jones, T. E.; Martinez Moreno, E.; Teschner, D.; Chernev, P.; Gliech, M.; Reier, T.; Dau, H.; Strasser, P. Unified structural motifs of the catalytically active state of Co(oxyhydr)oxides during the electrochemical oxygen evolution reaction. *Nat. Catal.* **2018**, *1*, 711–719.

[67] Bergmann, A.; Martinez-Moreno, E.; Teschner, D.; Chernev, P.; Gliech, M.; De Araújo, J. F.; Reier, T.; Dau, H.; Strasser, P. Reversible amorphization and the catalytically active state of crystalline Co_3O_4 during oxygen evolution. *Nat. Commun.* **2015**, *6*, 8625.

[68] Wang, H. S.; Abruña, H. D. Identifying adsorbed OH species on Pt and Ru electrodes with surface-enhanced infrared absorption spectroscopy through CO displacement. *J. Am. Chem. Soc.* **2023**, *145*, 18439–18446.